

SIRIUS: Dark matter cusp evolution in dense dwarf galaxies

Katsuhiro KANEKO,¹Takayuki R SAITO^{,2,3} Yutaka HIRAI,⁴ and Michiko S FUJII^{1,*}

¹Department of Astronomy, Graduate School of Science, The University of Tokyo, 7-3-1 Hongo, Bunkyo-ku, Tokyo 113-0033, Japan

²Department of Planetology, Graduate School of Science, Kobe University, 1-1 Rokkodai-cho, Nada-ku, Kobe, Hyogo 657-8501, Japan

³Center for Planetary Science (CPS), Graduate School of Science, Kobe University, 1-1 Rokkodai, Nada-ku, Kobe, Hyogo 657-8501, Japan

⁴Department of Community Service and Science, Tohoku University of Community Service and Science, 3-5-1 Iimoriyama, Sakata, Yamagata 998-8580, Japan

*E-mail: fujii@astron.s.u-tokyo.ac.jp

ORCID: 0000-0001-8226-4592, 0000-0002-5661-033X, 0000-0002-6465-2978

Abstract

Dwarf galaxies have a wide variety of structures, such as dark matter (DM) distribution, stellar-to-halo mass ratio, and stellar density. Recent high-resolution simulations have shown a variety of stellar-to-halo mass ratios for dwarf galaxies with a DM halo mass of $\sim 10^9 M_\odot$ at $z = 0$. In this study, we performed cosmological N -body/smoothed-particle hydrodynamic zoom-in simulations of dwarf galaxies with the highest gas and DM particle mass resolutions of $2.37 M_\odot$ and $12.8 M_\odot$, respectively. The stellar-to-DM halo mass ratio of one of our simulated dwarf galaxies was $\sim 10^{-4}$, typical for satellites of the Milky Way. The stellar mass ($10^5 M_\odot$) and half-mass radius (68 pc) were also similar to those of the satellites of the Milky Way. The power-law slope of the DM halo was $\alpha = -1.1$. On the other hand, the other simulated galaxy exhibited a stellar-to-halo mass ratio of $\sim 10^{-3}$ and a steeper power-law slope ($\alpha = -1.9$) than the other; the presence of baryonic matter deepened the cusp. The mass of $> 10^6 M_\odot$ and a half-mass radius of ~ 36 pc of this galaxy were similar to those of ultra-compact dwarf galaxies rather than the satellites of the Milky Way. This DM halo grew in mass earlier than the former one, and the central DM density was higher than that of the other even in the DM-only simulations.

Keywords: galaxies: dwarf — galaxies: formation — galaxies: evolution

1 Introduction

The Λ cold dark matter (Λ CDM) model has been widely accepted as the favored model to explain the formation of the large-scale structure of the Universe (Tegmark et al. 2004; Springel et al. 2005). Stars are formed in such dark matter (DM) halos, and galaxies evolve inside DM halos. The stellar mass depends on the halo mass, and the relation has been derived using abundance matching (e.g., Behroozi et al. 2013).

However, at the low-mass end ($M_h \lesssim 10^9 M_\odot$), which corresponds to the mass range of ultra-faint dwarfs, the stellar-to-halo mass ratio is still hardly determined from observations. The relation extrapolated from abundance matching of more massive galaxies shows a variation in the stellar-to-halo mass ratio (Behroozi et al. 2013; Moster et al. 2013; Sales et al. 2022). On the other hand, numerical studies have also been used to determine the stellar-to-halo mass ratio. Recent highest resolution simulations have reached the resolution of $4M_\odot$ for gas (Gutcke et al. 2021). However, the number of samples is not large. Lower mass resolution simulations with a few thousand M_\odot for gas particles have more samples, but their results do not agree with each other (Hopkins et al. 2018; Revaz & Jablonka 2018; Sales et al. 2022).

The structures of dwarf galaxies have also not yet been fully understood. The density profile of DM halos obtained from numerical simulations assuming the Λ CDM model showed a cuspy density profile in the central region ($\rho \propto r^{-1}$) (Navarro et al. 1996).

On the other hand, some observations of dwarf galaxies suggested a flat core ($\rho \sim \text{const.}$) in the innermost region of the DM halo (Flores & Primack 1994; Moore 1994; Burkert 1995; Oh et al. 2011) and known as the core-cusp problem (de Blok 2010).

Baryonic physics, such as star formation and supernova feedback, is one possible mechanism for creating a flat core. Governato et al. (2010) showed the formation of a core profile in cosmological hydrodynamic simulations. In their simulations, repeated gas accretion and removal due to supernova feedback after bursty star formation caused oscillations of gas potential and, as a result, transformed the cuspy density profile of the halo into a core (Pontzen & Governato 2012; Ogiya & Mori 2014; Bullock & Boylan-Kolchin 2017). Ogiya & Mori (2014) demonstrated that the repeated oscillation in the central region is crucial in causing the transition from a cusp to a core using their analytic calculations and N -body simulations.

Such a transition could occur in relatively massive dwarf galaxies. Di Cintio et al. (2014) reported that the cusp-core transition occurs when the stellar-to-halo-mass ratio is $\sim 10^{-3}$, but not when it is $\sim 10^{-4}$. Similar results were obtained in other simulation studies (Tollet et al. 2016; Lazar et al. 2020). However, the halo mass was more than $\sim 10^{10} M_\odot$ in these studies. In smaller galaxies, the duration of star formation is short, and therefore, the feedback energy may not be sufficient to form a DM core.

For lower mass dwarf galaxies, a higher resolution is required to resolve the small scale down to the central region. Wheeler

et al. (2019) performed cosmological zoom-in simulations for $2\text{--}9 \times 10^9 M_\odot$ dwarfs. Their mass resolution reached $30 M_\odot$, whereas the mass resolution of $> 10^{10} M_\odot$ galaxies in previous studies were $> 10^3 M_\odot$ (Di Cintio et al. 2014). The gravitational softening length was 14 pc. In their simulations, one of their dwarfs close to $10^{10} M_\odot$ achieved a stellar-to-halo mass ratio of $> 10^{-4}$ and had a core. This dwarf galaxy continued star formation beyond the reionization.

Another series of cosmological zoom-in simulations, EDGE, has been performed for DM halos with $\sim 10^9\text{--}10^{10} M_\odot$ at $z = 0$ using an adaptive mesh refinement (AMR) hydrodynamics code (Agertz et al. 2020). The finest spatial resolution reached 3 pc. Their mass resolution for star particles was $\sim 20 M_\odot$. In Orkney et al. (2021), they reported that mergers formed a core rather than repeated feedback and gas inflow. They also found a transition from cusp to core depending on the stellar mass fraction formed before and after the reionization (Muni et al. 2025). These results suggest that the long-term evolution of galaxies is essential for the DM halo structures of this mass range.

The recent highest resolution simulation, LYRA (Gutcke et al. 2021), also investigated the power of the DM distribution. Their simulation can resolve down to ~ 1 pc. Such a high resolution can resolve feedback due to the supernovae without a subgrid model (Hu 2019), different from low-resolution simulations (Revaz & Jablonka 2018; Hopkins et al. 2018). They did not find a correlation between the star formation activity and the shape of the DM halos in their simulations. They also reported that one of their models showed a central cusp deeper than that of their dark-matter only (DMO) simulation (Sureda et al. 2025).

On the other hand, recent observations have revealed a large scatter in the power of the central regions of the DM halos for the Milky Way (MW) satellite galaxies (Hayashi et al. 2020; Hayashi et al. 2023). Although the uncertainty is also large, the observed shape of the DM halos does not seem to depend on the stellar-to-halo mass ratio for dwarf galaxies. Oman et al. (2015) also showed that a diversity in the circular velocity of dwarf galaxies in their inner region compared to their simulations. This suggests that a diversity in DM halo distribution in dwarf galaxies. Thus, the structures of DM halos of dwarf galaxies, especially low-mass ones, still have uncertainties.

In this paper, we present the results of relatively low-mass ($\sim 10^9 M_\odot$ in DM) dwarf galaxy formation simulations with a mass resolution comparable to that achieved by Wheeler et al. (2019) and a spatial resolution comparable to that achieved by Agertz et al. (2020) to investigate the DM halo and stellar distributions. We have further resolved individual stars. The structure of this paper is as follows: Section 2 provides a description of our model and simulation setup. Section 3 presents the evolution of the cusp in our simulated dwarf galaxies. A comparison with observations and previous studies has been presented in Section 4. Section 5 summarizes this study.

2 Methods

2.1 Simulation Code

We performed the cosmological zoom-in simulations of dwarf galaxies using an N -body/smoothed-particle hydrodynamics (SPH) code, ASURA+BRIDGE (Saitoh et al. 2009; Hirai et al. 2021; Fujii et al. 2021). In this code, gravity was calculated using the tree method (Barnes & Hut 1986), and an opening angle of $\theta = 0.5$ was adopted. The hydrodynamics was computed using

the density-independent SPH (DISPH) method (Saitoh & Makino 2013). For radiative cooling and heating of the gas, metallicity-dependent cooling and heating functions from 10 K to 10^9 K generated by Cloudy ver. 13.05 (Ferland et al. 1998; Ferland et al. 2013; Ferland et al. 2017) were employed. We also adopted the UV background radiation model by Haardt & Madau (2012), combining the self-shielding model by Rahmati et al. (2013), and set the reionization due to UV background radiation to occur at $z = 8.5$, $t = 0.588$ Gyr. The chemical evolution of gas and stars was treated using the chemical evolution library CELIB (Saitoh 2017; Hirai et al. 2021).

For the gravitational softening lengths of the DM particles (ϵ_{DM}), we followed Hopkins et al. (2018):

$$\epsilon_{\text{DM}} = 30 \text{ pc} \left(\frac{m_{\text{DM}}}{1000 M_\odot} \right)^{\frac{1}{2}} \left(\frac{M_{\text{vir}}}{10^{12} M_\odot} \right)^{-0.2}, \quad (1)$$

where m_{DM} is the mass of the DM particles and M_{vir} is the virial mass of the system. A constant value of $M_{\text{vir}} = 10^9 M_\odot$ was used in our simulations. For those of gas, we followed Dutton et al. (2020) but modified the factor:

$$\epsilon_{\text{Gas}} = 2.13 \text{ pc} \left(\frac{m_{\text{gas}}}{1 M_\odot} \right)^{\frac{1}{3}} \left(\frac{\rho_{\text{th}}}{100 \text{ cm}^{-3}} \right)^{-\frac{1}{3}}, \quad (2)$$

where m_{gas} is the initial gas mass and ρ_{th} is the threshold density of star formation (see below). Initially, all the gas particles had the same mass, and the stars born in the simulations took over the softening length of the gas. The softening length for stars was set to be equal to that for the gas particles ($\epsilon_{\text{Star}} = \epsilon_{\text{Gas}}$). In the gravity calculation, the gravitational softening lengths ($\epsilon_{\text{soft}}^{\text{calc}}$) of DM and gas/star were varied by the redshift z ,

$$\epsilon_{\text{soft}}^{\text{calc}} = \begin{cases} \epsilon_{\text{soft}}, (z < z_f), \\ \epsilon_{\text{soft}} \times \frac{1+z_f}{1+z}, (z \geq z_f), \end{cases} \quad (3)$$

where $\epsilon_{\text{soft}} = \epsilon_{\text{soft}}^{\text{DM}}$ or $\epsilon_{\text{soft}}^{\text{Gas,Star}}$ and we employed $z_f = 9.0$.

2.2 Star formation and initial mass function

We adopted a star-by-star star-formation method (Hirai et al. 2021; Hirai et al. 2025), in which individual star particles have different masses following a given initial mass function (IMF). The formation of a star occurred when a gas particle satisfied the following conditions: (1) the divergence of velocity was less than 0 ($\nabla \cdot \mathbf{v} < 0$), (2) the gas number density was greater than 100 cm^{-3} , and (3) the temperature was less than 1000 K.

The star formation was assumed to probabilistically occur following the Schmidt law (Schmidt 1959; Katz 1992):

$$\frac{d\rho_*}{dt} = -\frac{d\rho_{\text{gas}}}{dt} = c_* \frac{\rho_{\text{gas}}}{t_{\text{dyn}}}, \quad (4)$$

where ρ_* , ρ_{gas} are a density of star and gas, respectively, c_* is a dimensionless star-formation efficiency, and $t_{\text{dyn}} = (4\pi G \rho_{\text{gas}})^{1/2}$ is a local dynamical time of the star formation region. From this relation, the probability of a gas particle forming a star in a time range of Δt was calculated as

$$p = \frac{m_{\text{gas}}}{\langle m_* \rangle} \left[1 - \exp \left(-c_* \frac{\Delta t}{t_{\text{dyn}}} \right) \right], \quad (5)$$

where $\langle m_* \rangle$ is the average stellar mass of the IMF. A random number $0 \leq R < 1$ was generated when a gas particle satisfied the three criteria. If $R < p$, a stellar particle was created (see Hirai et al. 2021 for more details). In this study, we adopted $c_* = 0.5$ following previous simulations by Saitoh et al. (2008).

Once a star-forming region was identified, a stellar mass was drawn following a given mass function. We adopted a Salpeter IMF (Salpeter 1955) but modified it to reduce the number of particles of low-mass stars. We adopted a modified IMF (hereafter cutoff IMF), in which stars with $m_\star < 1M_\odot$ were summarized as superparticles with $1.0 \leq m_\star/M_\odot \leq 1.1$. The mass function was expressed as:

$$\frac{dN}{d\log_{10} m_\star} \propto \begin{cases} m_\star^{-1.35}, & (1.1 < m_\star/M_\odot < 120), \\ \frac{1}{1.1-1.0M_\odot} \int_{0.1M_\odot}^{1.1M_\odot} m_\star^{-1.35} dm_\star, & (1.0 \leq m_\star/M_\odot \leq 1.1). \end{cases} \quad (6)$$

With this cutoff IMF, the number of low-mass stars was reduced, thus maintaining the mass fraction of massive stars in the entire mass distribution.

The stellar mass was also limited by the local gas mass to conserve the local mass. If the mass drawn from the IMF was smaller than that of the gas particle, the star could be born from the gas particle. Even if the stellar mass was larger than the mass of the parental gas particle, we searched the gas mass within $r_{\max} = 3\text{pc}$. If the gas within r_{\max} was twice as massive as the selected stellar mass, a star particle was formed by collecting the stellar mass from the gas particles within r_{\max} . If not, a new stellar mass was drawn. The center of mass of the gas particles determined the position and velocity of the star particle.

2.3 Stellar evolution and feedback

Stellar evolution and feedback were also treated with CELIB. Lifetimes of star particles were determined from the metallicity-dependent stellar lifetime table in Portinari et al. (1998). Instead of calculating radiation transfer, we assumed that massive stars ($> 15M_\odot$) formed spherical HII regions. We calculated each Strömgren radius, which is the radius of the HII region of the star, using the local gas density, and provided thermal energy to maintain the temperature within the Strömgren radius 10,000 K (Fujii et al. 2021). The maximum extent of HII regions was set to 30 pc from the center to prevent the HII region from expanding too large in almost gas-free regions in the simulation (Fujii et al. 2021).

Following the yield table of Nomoto et al. (2013), stars within the mass range of $13 \leq m_\star/M_\odot \leq 40$ exploded as core-collapse supernovae when they reached the end of their lives. We assumed that these supernovae released energy of 10^{51} erg. We also assumed that 5% of stars of $20-40M_\odot$ exploded as broad-line Type Ic supernovae (hypernovae) and released energy of 10^{52} erg. We adopted a simple supernova feedback model that injects all supernova energy as thermal energy into the surrounding gas particles. We did not include other stellar feedback such as Type Ia supernovae because the gas was removed mainly due to reionization before such feedback is activated.

2.4 Initial Conditions

As a first step, we performed a DM-only cosmological simulation of a $4\text{Mpc}h^{-1}$ box. The initial condition was generated by MUSIC (Hahn & Abel 2011). We assumed a flat ΛCDM cosmology and set cosmological parameters as the values obtained from Planck Collaboration et al. (2020) ($H_0 = 67.32$, $\Omega_{\text{m}0} = 0.3158$, $\Omega_{\Lambda0} = 0.6842$, and $\Omega_{\text{b}0} = 0.04939$). The mass resolution of the low-resolution cosmological simulation was $m_{\text{DM}} = 5 \times 10^5 M_\odot$. Starting from $z = 100$, we performed a cosmological simulation

Table 1. Halo properties at $z = 0$. Note that V_{\max} is the maximum circular velocity.

Halo Number	$M_{\text{vir}} [M_\odot]$	$R_{\text{vir}} [\text{kpc}]$	$V_{\max} [\text{km/s}]$
230	1.075×10^9	21.75	18.54
284	8.78×10^8	20.29	17.70

Table 2. Resolution of the simulations

Model	$m_{\text{gas}} [M_\odot]$	$\epsilon_{\text{gas}} [\text{pc}]$	$m_{\text{DM,min}} [M_\odot]$	$\epsilon_{\text{DM,min}} [\text{pc}]$
DMO	-	-	1.21×10^2	13.8
Hydro Low	1.21×10^3	22.7	6.55×10^4	102
Hydro	1.90×10^1	5.68	1.02×10^2	12.7

From left to right: (1) gas-mass resolution (m_{gas}), (2) gas softening length (ϵ_{gas}) (3) minimum dark-matter mass ($m_{\text{DM,min}}$) (4) minimum dark-matter softening length ($\epsilon_{\text{DM,min}}$).

using GADGET-2 (Springel 2005) up to $z = 0$. Amiga's Halo Finder (AHF; Knollmann & Knebe 2009) was used to detect DM halos at $z = 0$, and then the DM halos with $M_{\text{halo}} \simeq 10^9 M_\odot$ at $z = 0$ in isolated environments were selected. For the isolated condition, we adopted no more than 10 times massive DM halos within 1 Mpc.

Using MUSIC, the refined initial conditions of the selected halos were generated. The zoom-in region was determined by the following method (cf. Griffen et al. 2016): (1) Pick up particles within $4R_{\text{vir}}$ from a halo center at $z = 0$. (2) Determine an ellipsoid region such that all of these particles at $z = 100$ are included. (3) The region whose size is multiplied by 1.05 is the zoom-in region for reducing the contamination of the coarse boundary particles. Low-resolution zoom-in simulations were performed with $m_{\text{gas}} \sim 1.2 \times 10^3 M_\odot$ and $m_{\text{DM}} \sim 6.5 \times 10^3 M_\odot$ using ASURA+BRIDGE. Hereafter, we refer to them as Hydro Low models. From the results of this test, the most and least massive dwarf galaxies in stellar mass (Halo 284 and Halo 230, respectively) were chosen for higher-resolution simulations. Their surroundings and the DM distributions are shown in Figure 1. Table 1 summarizes the properties of Halo 230 and Halo 284 at $z = 0$ obtained with AHF.

For Halo 230 and Halo 284, high-resolution zoom-in simulations were performed with $m_{\text{gas}} = 19.0 M_\odot$ and $m_{\text{DM}} = 102 M_\odot$, and we refer to them as Hydro models. The Hydro model simulation was continued up to $z = 0.5$ for Halo 230, whereas for Halo 284, it was continued until $z = 0.32$ because it experienced a merger around $z = 0.5$. For comparison, we also performed simulations without gas, and we refer to them as DM-only (DMO) models. The mass resolution of this simulation was the same as that of the Hydro models. The resolution is summarized in Table 4.

In addition, we performed a higher-resolution simulation for only Halo 284 up to $z = 8.72$, which we refer to as the Hydro High model (see Appendix 1). The mass resolution of this model was $2.37 M_\odot$, which was sufficiently high to resolve the supernova explosions (Hu 2019). Due to our limited computational resources, we terminated this simulation at $z = 8.72$ and investigated the convergence at this point in time.

2.5 Determination of the halo center

In order to determine the DM density profiles of the simulated dwarf galaxies, the shrinking sphere method (Klypin & Holtzman

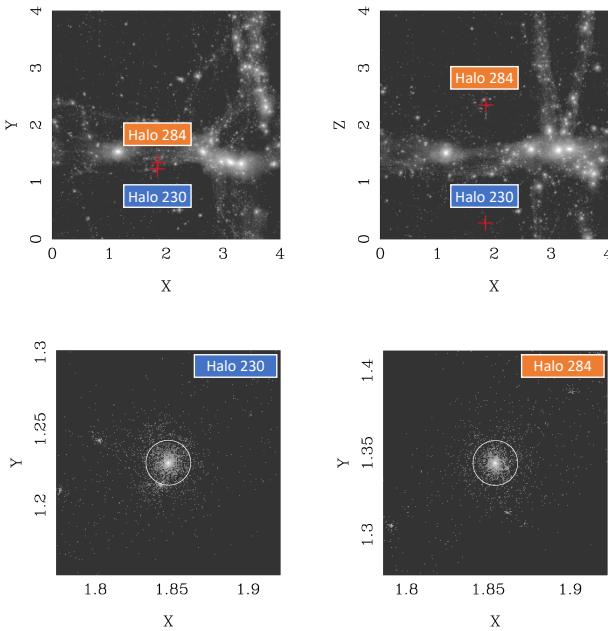


Fig. 1. Top panels: Dark matter surface density distribution, and the positions of Halo 230 and Halo 284 in it. The red crosses show the centers of the halos at $z = 0$. Bottom panels: Zoomed-in images of each halo. The white circles show the virial radii. Axis scales are in Mpc/h for all panels. Alt text: Four-by-four panel figure. The top panels show the positions of Halo 230 and 284 in a four comoving megaparsec square scale large-scale distribution of dark matter surface density in x-y (left) and x-z (right) planes. Bottom panels show zoomed-in images of Halo 230 (left) and Halo 284 (right).

1997; Power et al. 2003; Navarro et al. 2004; Fitts et al. 2017) was used. First, a sphere with the center and virial radius calculated with AHF was considered. Next, the center-of-mass position of the DM particles within the sphere was calculated, and the center of the sphere was moved there. Then, the radius of the sphere was reduced by 2.5%. This operation was repeated until the number of DM particles in the sphere was less than 1000. The virial mass, radius, and radial profiles were calculated using the center determined with this method. Here, the virial radius was the radius within which all stars were bound to the halo, and the mass was the total mass within the virial radius.

3 Results

3.1 Halo mass evolution and star formation

In Figure 2, we present the distribution of the DM and stars at $z = 0.5$. At this time, the star formation has already finished, and the dwarf galaxies are gas-free. Stars are concentrated in the central region of the main DM halo.

The halo virial mass evolution is shown in Figure 3. The virial mass and radius were calculated using the center derived by the method described in Section 2.5. Because of the existence of baryons, the virial masses of the Hydro and Hydro Low models are less than those of the DMO models. As shown in this figure, the halo virial mass and radii did not strongly depend on the resolution.

Figure 4 shows the time evolution of the star formation rate av-

eraged over 50 Myr. Star formation rates were calculated using an archaeological method (e.g., Fitts et al. 2017) as follows: First, the member stars within $0.5 R_{\text{vir}}$ of each halo at 8.56 Gyr for Halo 230 and 10.1 Gyr for Halo 284 were selected. Then, their formation epoch was calculated from their stellar age. Finally, the star formation rate of this dwarf was calculated based on the ages of its member stars.

The Halo 230 Hydro model showed a single-peak star formation history. The star formation started earlier than the reionization epoch and ended around 1 Gyr. No further star formation occurred beyond this time, although the halo mass continued to increase via mergers and accretions at later times (see Figure 3). On the other hand, in the Hydro Low model, the star formation started around the reionization epoch and continued slightly later in time. The final mass and the half-mass radius of the stars were $1.23 \times 10^5 M_{\odot}$ and 68.3 pc, respectively (see Table 3).

For Halo 284, the Hydro and Hydro Low models showed a single-peaked star formation history similar to that of Halo 230, but a small star formation occurred again at ~ 1.4 Gyr. Further, around 8–10 Gyr, Halo 284 experienced a major merger, but no star formation occurred at this time. The star formation rate of Halo 284 was an order of magnitude higher than that of Halo 230. The final stellar mass of Halo 284 ($2.12 \times 10^6 M_{\odot}$) was an order of magnitude higher than that of Halo 230. However, the half-mass radius of the star for Halo 284 was only 36.4 pc, which is smaller than that for Halo 230. Thus, Halo 284 is more compact compared to Halo 230.

The difference between Halo 230 and Halo 284 appears to stem from the variation in their halo mass evolution. Figure 5 shows the time evolution of the maximum halo circular velocity measured using AHF and the corresponding virial temperature. The circular velocity of Halo 284 started to increase earlier than that of Halo 230, although the final circular velocities were similar for both halos. This difference led to earlier star formation and a higher star formation rate in Halo 284. Okamoto & Frenk (2009) showed that halos with a circular velocity above 12 km s^{-1} , i.e., $5 \times 10^3 \text{ K}$ can retain gas over the reionization epoch. The circular velocity of Halo 284 exceeds this threshold, but that of Halo 230 does not. In Okamoto & Frenk (2009), halos below this threshold did not form stars at all, but our model forms stars. This may be due to a higher resolution of our simulations compared to theirs, and therefore, Halo 230 may also have locally reached a density high enough for star formation. Indeed, the timing of the first star formation tends to delay as the resolution decreases (see Figure 4).

Compared to the Hydro and Hydro Low models, the star formation rates of the low-resolution models were always lower than those of the high-resolution ones. Consequently, the resulting stellar mass was higher for higher resolution models. On the other hand, the half-mass radius of stars decreased with higher resolution. The stellar half-mass radius of Halo 284, the model with a larger M_{\star}/M_{vir} , shrank more (from 178 to 36 pc) with a higher resolution compared to Halo 230 (from 118 to 68 pc). We also tested a case with even higher resolution ($2.37 M_{\odot}$ for gas particles), although the simulation was run only to $z = 8.72$ ($t = 0.568$ Gyr). The comparison is shown in Appendix 1.

We also followed the time evolution of the density distribution of each component. Figures 6 and 7 present the time evolution of the radial profiles of each component of Halo 230 and Halo 284 Hydro models, respectively. Once stars formed, the HII region appeared, and a fraction of the gas was heated to 10^4 K . Supernovae also occurred, but their energy was insufficient to stop star formation at this moment. The gas density inside the galaxies was

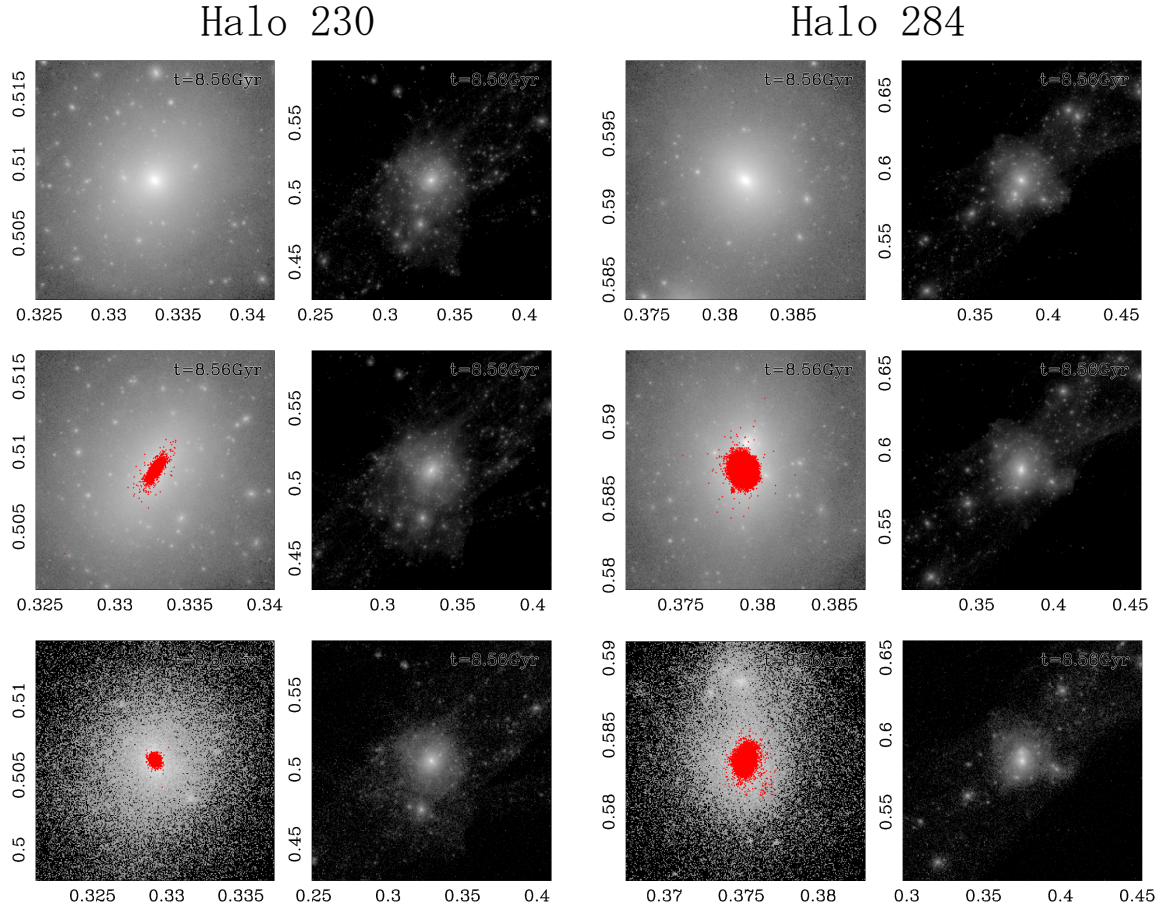


Fig. 2. DM surface density distributions of Halo 230 (left) and Halo 284 (right) at $z = 0.5$. From top to bottom, each row represents the results of the DMO, Hydro, and Hydro Low models, respectively. The left and right columns of each halo show the DM surface density within $0.5 R_{\text{vir}}(t)$ and $5 R_{\text{vir}}(t)$ from the halo center, respectively. The red dots in the left column indicate star particles. Axis scales are in Mpc/h for all panels. Alt text: Twelve-panel grayscale images of the dark matter surface density centered on the halo center. Red dots are plotted on the grayscale images for the Hydro and Hydro Low models.

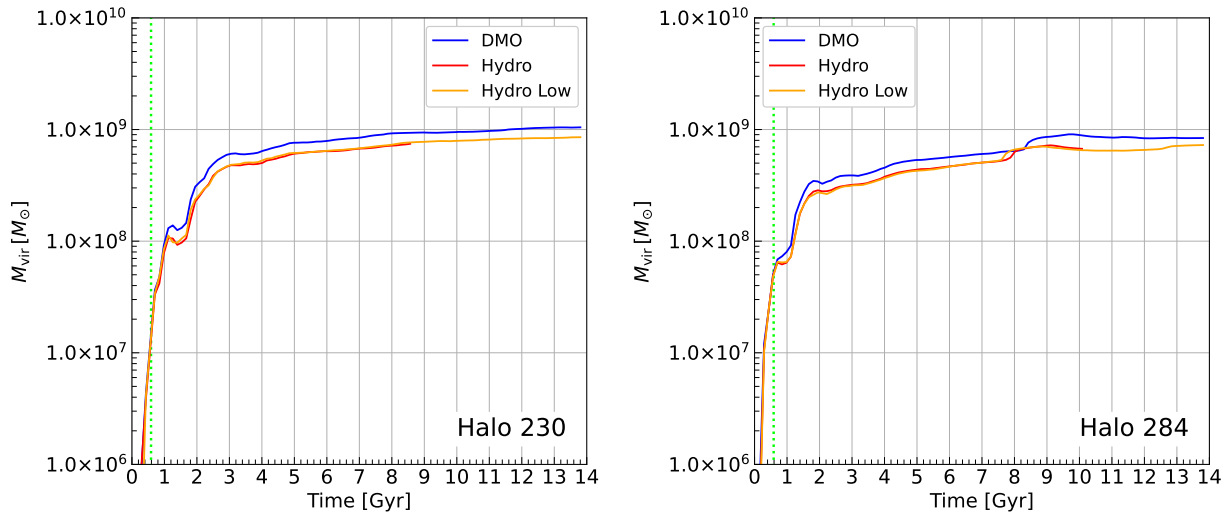


Fig. 3. Time evolution of the viral mass of the halo (M_{vir}) for Halo 230 (left panel) and Halo 284 (right panel). The green dotted vertical line indicates the reionization epoch assumed in this simulation ($z = 8.5$, $t = 0.588 \text{ Gyr}$). Alt text: Two line graphs. The range of the x-axis (time) is zero to fourteen gigayears. Blue and red lines are for DMO and Hydro runs, respectively. The virial masses increase with time and reach the final mass at around eight point five gigayears.

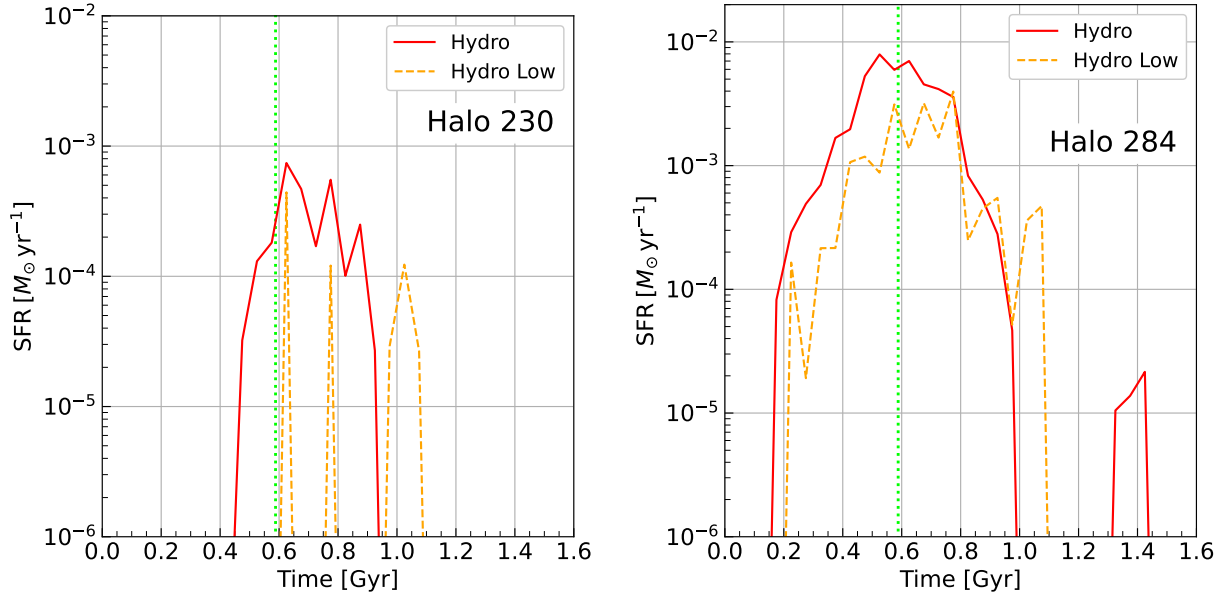


Fig. 4. Star formation histories of Halo 230 (left) and Halo 284 (right). Star formation rates are averaged over 50 Myr. The green dotted line indicates the reionization epoch. Alt text: Line graphs peaked at around the reionization epoch. The red and orange lines correspond to the Hydro and Hydro Low models, respectively. The peak value of the star formation rate of Halo 230 is slightly less than ten to the minus three solar mass per year. The peak value of Halo 284 is slightly less than ten to the minus two solar masses per year.

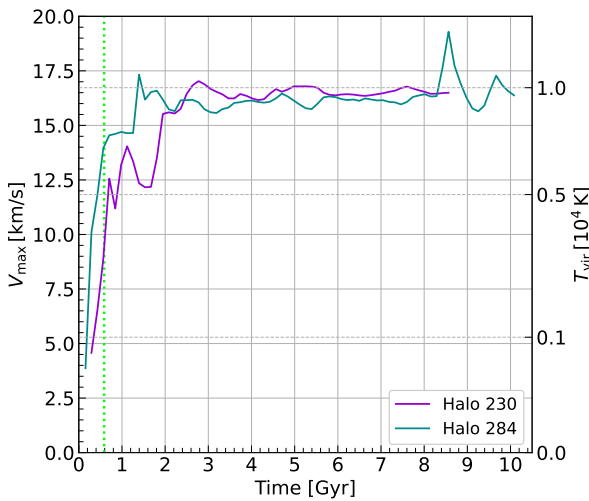


Fig. 5. Time evolution of V_{\max} and T_{vir} in each simulation. The left axis shows the maximum circular velocity, whereas the y -axis ticks on the right side show the virial temperature. The green dotted line represents the time at which reionization occurs in this simulation. Alt text: Line graph with two lines. Purple and green lines are for Halo 230 and 284, respectively. The X-axis indicated the time in gigayears. Left and right y -axes show the circular velocity and the corresponding virial temperature, respectively. The circular velocity increases with time and reaches a circular velocity of approximately 17 kilometers per second. The circular velocity corresponds to ten thousand kelvin.

maintained to be high enough to continue star formation. After the reionization epoch ($z = 8.5$, $t = 0.586$ Gyr), the gas in the outer region of the galaxies was heated to more than the escape velocity, and the gas component started to decrease.

In Halo 230, the gas dominated the stars in the innermost region until $t = 0.706$ Gyr (before the reionization in our simulation). At $t = 0.844$ Gyr, the gas in the central region started to decrease, and the stars became dominant. At $t = 1.120$ Gyr, the gas was depleted, and star formation ended.

In Halo 284, the star formation started earlier than in Halo 230, and the stars dominated both gas and DM in the central region at $t = 0.568$ Gyr, which is before the reionization epoch. Since the central gas density was high enough at this moment, Halo 284 continued star formation after stars dominated the central region. The reionization contributed to evaporating the gas, but star formation continued even after the reionization epoch. The gas of the central region was finally depleted at $t = 1.120$ Gyr.

We measured the properties of the halo and stellar distribution at $z = 0.5$. The results are summarized in Table 3. The halo virial mass and radius were calculated with the center determined using the method described in Section 2.5. The ratio of stellar to halo virial masses (M_{\star}/M_{vir}) was 1.65×10^{-4} for the Halo 230 Hydro model, which is similar to the satellites of the Milky Way. In contrast, M_{\star}/M_{vir} of Halo 284 (3.05×10^{-3} for Hydro) was an order of magnitude higher than that of Halo 230. This is a typical value for galaxies that are more massive than the satellites of the Milky Way (Lazar et al. 2020).

3.2 DM density profile

Figure 8 presents the density profiles at $t = 8.56$ Gyr and $t = 8.29$ Gyr for Halo 230 and Halo 284 Hydro models, respectively. Because Halo 284 underwent a merger around the final snapshot, we adopted a snapshot taken before the merger. For comparison,

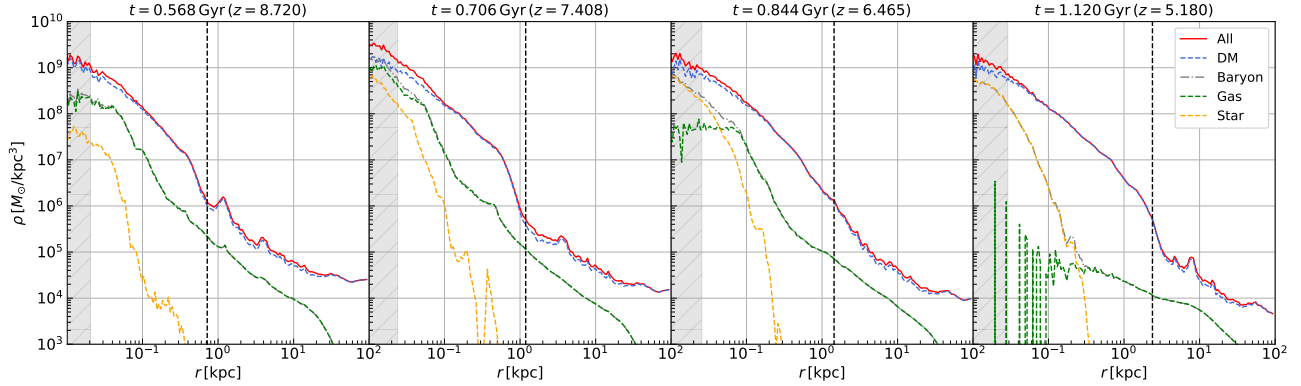


Fig. 6. Radial distribution of the density (ρ) of each component of the Halo 230 Hydro model from the early stage of star formation ($t = 0.568$ Gyr) to the end of star formation ($t = 1.120$ Gyr). The gray region shows the convergence radius obtained with eq. (A1) and the black dashed vertical line indicates the virial radius. Alt text: Three-panel figure with four lines for each panel. Red, blue, gray, green, and yellow indicate total, DM, baryon, gas, and star components. The density decreases with radius. The panels are for 0.568, 0.706, 0.844, and 1.120 gigayears.

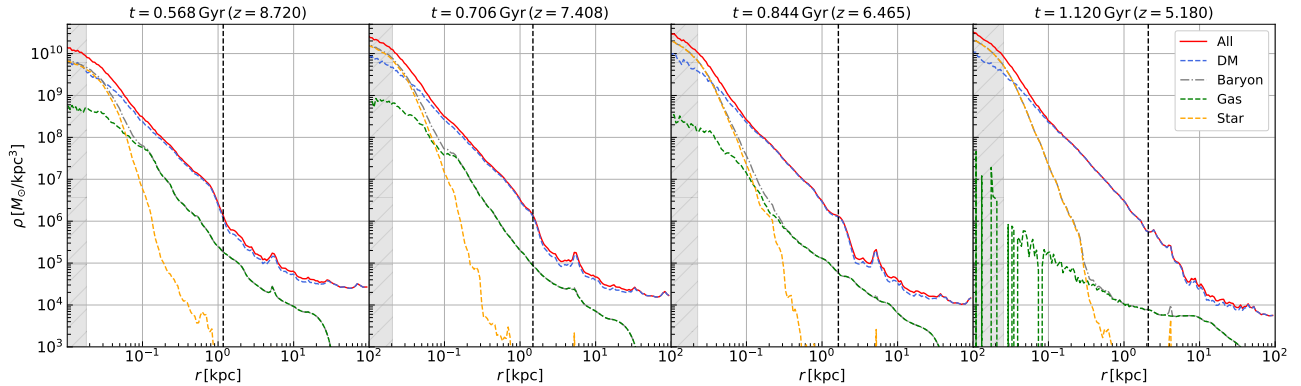


Fig. 7. Same as 6 but for Halo 284. Alt text: Three-panel figure with four lines for each panel. Red, blue, gray, green, and yellow indicate total, DM, baryon, gas, and star components. The density decreases with radius. The panels are for 0.568, 0.706, 0.844, and 1.120 gigayears.

Table 3. Properties of the dwarf galaxies at $z = 0.5$.

Halo Number	Model	$M_{\text{vir}} [M_{\odot}]$	$R_{\text{vir}} [\text{kpc}]$	$M_{\star} [M_{\odot}]$	$R_{1/2}^{3D} [\text{pc}]$	$\bar{R}_{1/2}^{2D} [\text{pc}]$	$V_{\text{max}} [\text{km/s}]$	M_{\star}/M_{vir}
230	DMO	9.34×10^8	17.2	-	-	-	18.5	-
	Hydro	7.45×10^8	15.9	1.23×10^5	68.3	52.7	16.5	1.65×10^{-4}
	Hydro Low	7.66×10^8	16.1	3.45×10^4	117.7	90.7	16.7	4.50×10^{-5}
284	DMO	8.07×10^8	16.3	-	-	-	18.1	-
	Hydro	6.95×10^8	15.5	2.12×10^6	36.4	28.4	19.3	3.18×10^{-3}
	Hydro Low	6.94×10^8	15.5	8.97×10^5	178.2	137.9	17.0	1.29×10^{-3}

From the third onward: (1) halo virial mass, (2) halo virial radius, (3) stellar mass within $0.2R_{\text{vir}}$, (4) three-dimensional half-stellar-mass radius, (5) projected half-stellar-mass radius, (6) maximum circular velocity, and (7) $M_{\star} - M_{\text{vir}}$.

the DM profiles of the DMO models are also shown in the figure, but we reduced the mass by 15.6 % as the baryon mass. For Halo 230, the DM halo profile remained unchanged regardless of the baryonic components. In contrast, for Halo 284, the DM halo density increased significantly in the innermost region, along with the baryonic components.

We evaluated the power-law slope (α) of the innermost region of the density profile. In this study, the power-law slope was defined to be between the convergence radius (eq. A1) and twice that radius similar to Sureda et al. (2025). Previous studies (Di Cintio et al. 2014; Tollet et al. 2016; Lazar et al. 2020) used the power-law slope at 1–2 % of the virial radius at $z=0$ ($R_{\text{vir}}(z=0)$). However, in our simulations, 1–2 % of $R_{\text{vir}}(z=0)$ was too far from the central region (see Appendix 2). The density profiles and fitted α at $z=0.5$ are shown in Figure 8. We obtained $\alpha = -0.88$ and -1.07 for the Hydro and DMO models of Halo 230, respectively. As can also be seen from the density profiles, the powers did not change much with the existence of the baryonic components. For Halo 284, we obtained $\alpha = -1.94$ and -1.45 for the Hydro and DMO models, respectively. Thus, Halo 284 is more cuspy with baryonic components. This is due to the dense stellar components in the central region of Halo 284. As seen in Figure 7, Halo 284 is baryon-dominant in the central region. This made the central potential deeper, and as a result, the DM density also increased.

In both halos, we did not find any clear cores of DM distribution as was pointed out in previous simulations (e.g., Tollet et al. 2016; Fitts et al. 2017; Wheeler et al. 2019; Orkney et al. 2021). This could be because of the very small halo mass compared to previous studies. For example, the halo mass in the study of Wheeler et al. (2019) is close to $10^{10} M_{\odot}$. Massive halos have deeper potentials and therefore can cause multiple starbursts, which are necessary to make the transition from cusp to core. Muni et al. (2025) pointed out that the amount of star formation that occurs earlier than the reionization epoch deepens the DM halo potential, as seen in our Halo 284. They also showed that the star formation occurring later than the reionization epoch is crucial for creating a core. However, both of our models ended star formation just after the reionization epoch.

3.3 Time evolution of the power-law slope

We investigated the time evolution of the power-law slope (α) because it may evolve with time, as shown in the study by Tollet et al. (2016). The results are shown in Figure 9. After the last merger event at approximately 3–4 Gyr, the power-law slope did not change significantly for the DMO and Hydro models. Averaging the slope of $t = 5$ –8.5 Gyr, we defined the final slope as $\alpha = -1.01 \pm 0.01$ for the Hydro model.

In contrast, the power-law slope of the Hydro model of Halo 284 largely decreased in the first 2 Gyr, in which the star formation occurred. During this period, the power-law slopes of the DMO and Hydro models were largely distinct, and the power of the Hydro model reached -2.0 . The power-law slope of the DMO model gradually decreased from -1.1 to -1.4 with time. This is due to the increase of the convergence radius with time (see eq. A1). This halo experienced a merger at approximately 10 Gyr. After that, the power was almost constant. On the other hand, the power-law slope of the Hydro model increased from -2.0 to -1.9 with time. Compared to the two halos, Halo 284 always had a steeper slope than Halo 230, even for the DMO models. Averaging the slope of $t = 8$ –10 Gyr, we obtained $\alpha = -1.90 \pm 0.01$ for the Hydro Model. The decrease in α of the Halo 284 DMO model may be due to the

change in the convergence radius with time.

4 Discussion: comparison with observations and previous simulations

4.1 Dark matter distribution

Figure 10 shows the relationship between the stellar-to-halo mass ratio ($M_{\star}/M_{\text{halo}}$) and α obtained from our simulations, observed dwarf galaxies (Hayashi et al. 2020; Hayashi et al. 2023), and previous simulations (Di Cintio et al. 2014; Tollet et al. 2016; Lazar et al. 2020). For the previous simulations, we fitted functions to their results and plotted the regions shown in the figure. The details of this process are described in Appendix 3. For the observations, fittings were performed using the Hernquist profile in ellipsoidal geometry (Hayashi et al. 2020; Hayashi et al. 2023), whereas simulations assumed a spherical model.

Halo 230 is consistent with those obtained from observations and previous simulations. On the other hand, the value of α for Halo 284 is significantly smaller than those obtained from previous simulations, and $M_{\star}/M_{\text{halo}}$ is much higher than those of the satellites of the Milky Way. We note that the dwarf galaxies with $M_{\star}/M_{\text{halo}} \sim 3 \times 10^{-3}$ in previous simulations typically have a DM halo with a mass of 10^{10} – $10^{11} M_{\odot}$, whereas Halo 284 has $\sim 10^9 M_{\odot}$.

In the sample of Sureda et al. (2025), which is a simulation with the mass resolution of $4M_{\odot}$, there was a dwarf galaxy which shows a stellar-to-halo mass ratio similar to that of Halo 284. It (their Halo A) also showed a high stellar-to-halo mass ratio of order of 10^{-3} , similar to our Halo 284. Their Halo A showed a deeper cusp in the hydrodynamical simulation than in the DMO simulation. However, the stellar distribution in their simulation had a mass of $\sim 10^7 M_{\odot}$ and a half-mass radius of ~ 300 pc. They are an order of magnitude larger than our Halo 284.

In the samples in Orkney et al. (2021), they showed that the dark matter density in the central region with baryons decreased compared to DMO simulations due to the baryon physics, and the degree of the decrease becomes larger in more massive halos. On the other hand, we did not see any decrease in the dark matter density, although our sample size is only two. However, their halo masses are $> 1.3 \times 10^9 M_{\odot}$, which is more massive than our simulations ($< 10^9 M_{\odot}$).

Kaneda et al. (2024) proposed a condition for the transition from cusp to core based on the DM halo density in the central region rather than the stellar-to-halo mass ratio. Hayashi et al. (2025) showed the relation between the maximum rotation speed, which indicates the halo mass, and the DM halo density in the central region of the observed dwarf galaxies. The observation aligns more closely with the simulation than with the stellar-to-halo-mass ratio. We plotted the same relationship between our simulated galaxies and observations (Hayashi et al. 2020; Hayashi et al. 2023) and previous simulations (Lazar et al. 2020) in Figure 11. In this plot, some ultra-faint and ultra-diffuse galaxies show dark matter surface densities as high as those of Halo 284.

4.2 Stellar distribution

We also compared the stellar mass and half-mass radius with those of the Milky Way globular clusters and dwarf galaxies, along with ultra compact dwarfs (UCDs), in Figure 12. Halo 230 was close to the satellites of the Milky Way, but had a slightly smaller half-mass radius. This mass-radius relation is consistent with Halo 284

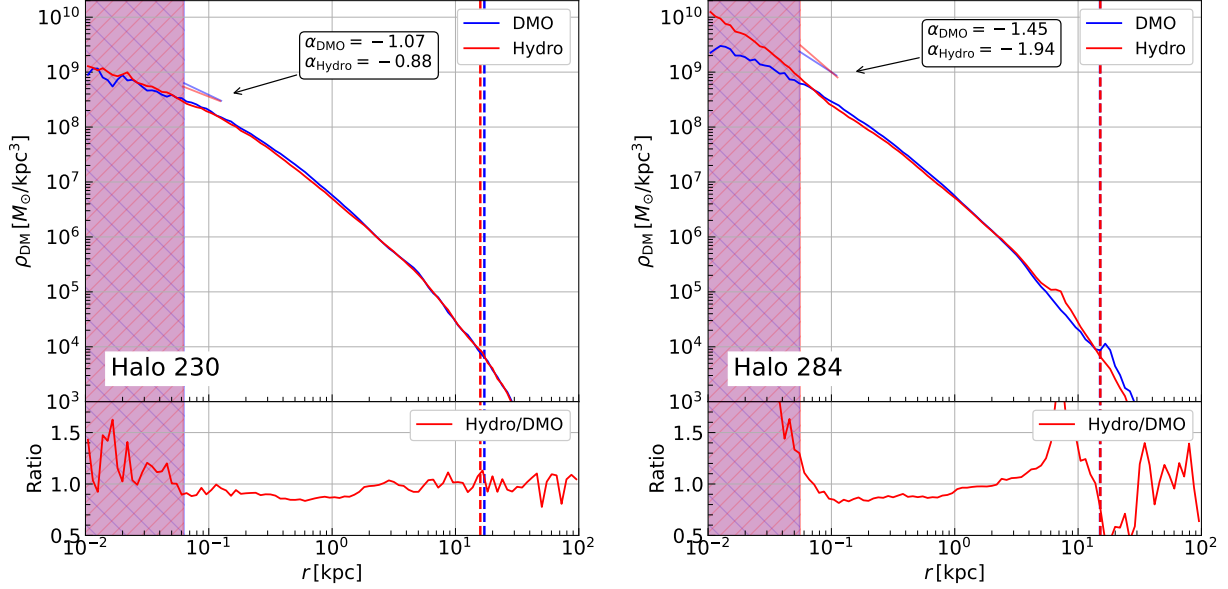


Fig. 8. Top panel: density profiles of the DM halo of the Hydro and DMO models (top panel) for Halo 230 (left) and Halo 284 (right) at $t = 8.56$ Gyr ($z = 0.50$) and $t = 8.29$ Gyr ($z = 0.54$), respectively. The colored regions indicate the convergence radii (R_{conv}). The vertical dashed lines indicate the virial radii. The red and blue lines above the profiles indicate the slopes obtained from power-law fitting to $1 - 2R_{\text{conv}}$ for the DMO and Hydro models, respectively. Bottom panels: the ratio of Hydro and DMO models. Alt text: Two-panel figures that include two panels. Two-line figure (top panel) and one-line figure (bottom) for each. In the top panels, blue and red indicate DMO and Hydro models, respectively. The fitted powers are -1.07 and -0.88 for the DMO and Hydro models of Halo 230. They are -1.45 and -1.94 for the DMO and Hydro models of Halo 284.

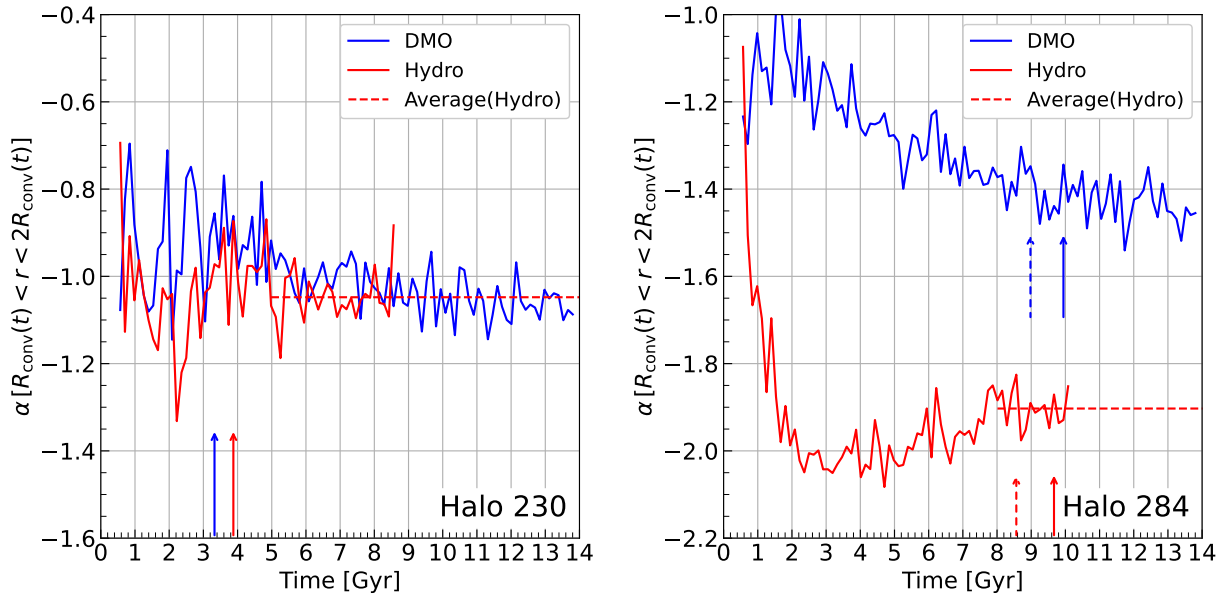


Fig. 9. Time evolution of the slopes obtained from the power-law fitting to $1 - 2R_{\text{conv}}(t)$ for Halo 230 (left) and Halo 284 (right) models. The red and blue curves indicate the Hydro and DMO models, respectively. The red dashed line indicates the slope averaged in 5.00–8.56 Gyr for Halo 230 ($\alpha = -1.01$) and 8.01–10.1 Gyr for Halo 284 ($\alpha = -1.90$). The dashed and solid arrows indicate the time of close encounters and mergers, respectively. Alt text: Two-line figures. In the left panel, blue and red arrows at 3.2 and 4 gigayears. In the right panel, blue dashed and full arrows are at 9 and 11 gigayears. Red dashed and full arrows are at 8.5 and 9.5 gigayears.

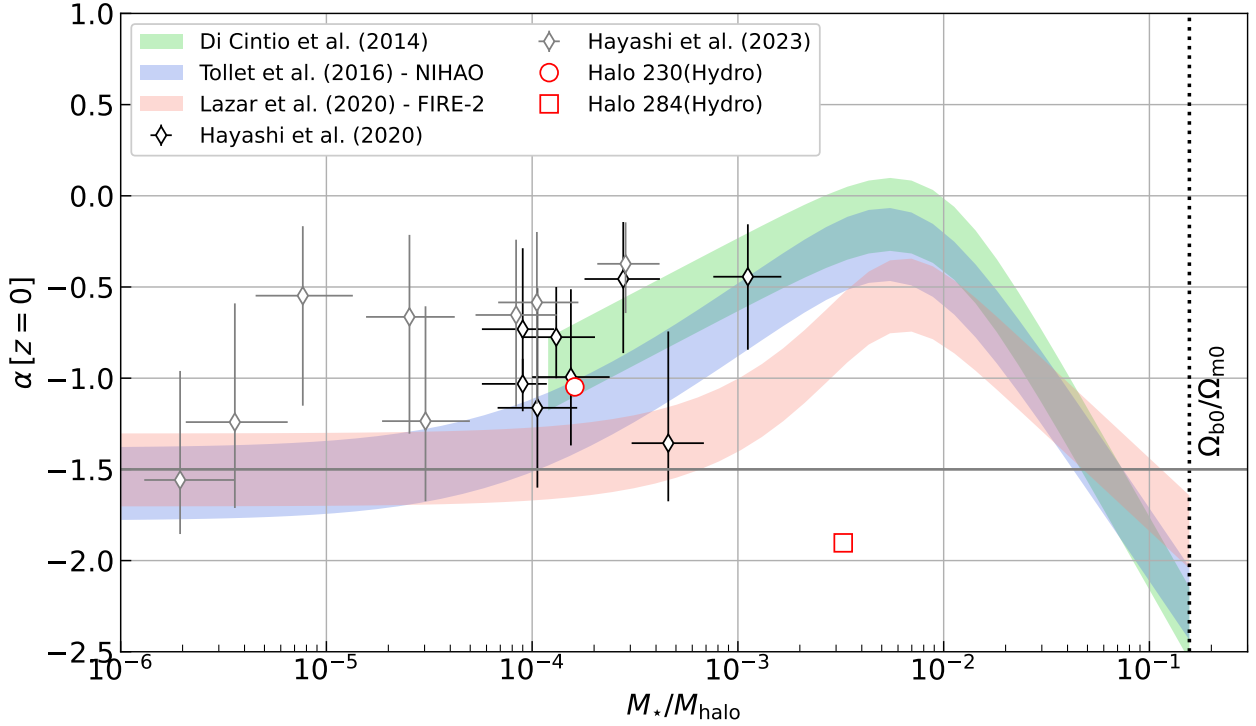


Fig. 10. Relationship between the stellar-to-halo mass ratio (M_*/M_{halo}) and the inner power-law slope of DM halo (α). The green, blue, and red ranges are the relationships obtained from the simulation results of Di Cintio et al. (2014), Tollet et al. (2016), and Lazar et al. (2020), respectively, and the vertical width of the ranges for all is $\Delta\alpha = 0.2$. The diamonds with error bars represent the observations of dwarf galaxies (Hayashi et al. 2020; Hayashi et al. 2023). The red circle and square indicate the results of the Hydro models for Halo 230 and Halo 284, respectively. Note that α of the Hydro models is the average value of earlier times (see Fig. 9). Alt text: Scatter plot with three shaded regions.

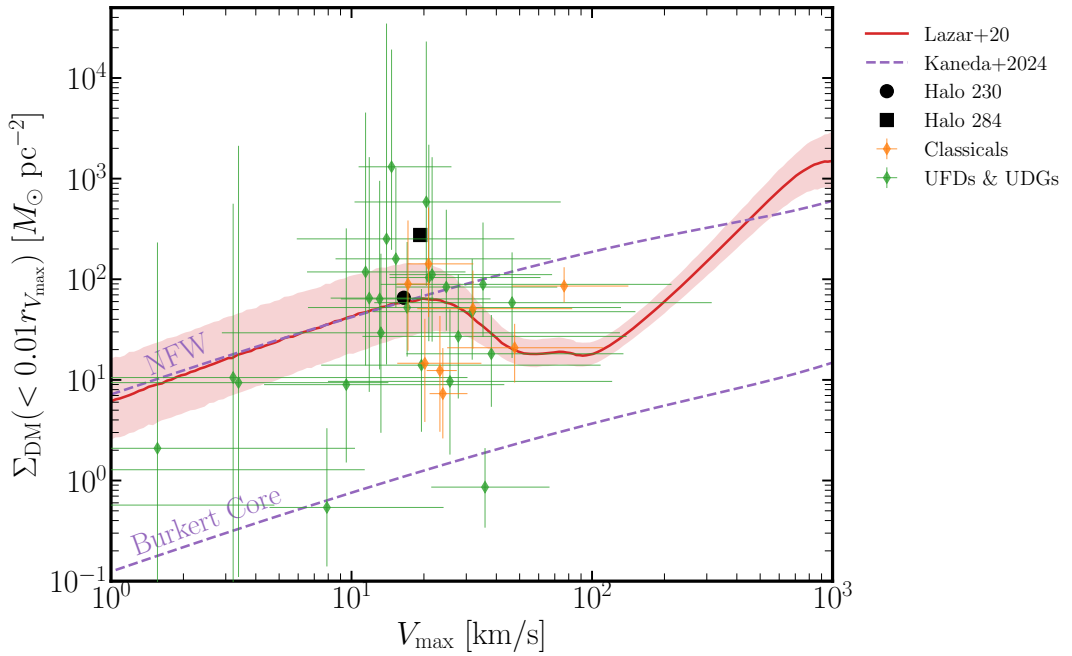


Fig. 11. Central surface density of the DM halo within 1 % of the radius of the maximum circular velocity, $\Sigma_{\text{DM}}(< 0.01r_{V_{\text{max}}})$ as a function of the maximum circular velocity, V_{max} . The diamonds with error bars show the observed dwarfs; the orange diamonds indicate classical dwarfs associated with the Milky Way (Hayashi et al. 2020), whereas the green ones indicate ultra-faint dwarfs and ultra-diffuse galaxies (Hayashi et al. 2023). The red line indicates the result of Lazar et al. (2020). The red shaded region shows the 1σ dispersion. The two purple dashed lines represent the predictions from Kaneda et al. (2024) for the NFW (cuspy) and Burkert (cored) profiles, respectively. Alt text: Scatter plot with three lines and a shaded region.

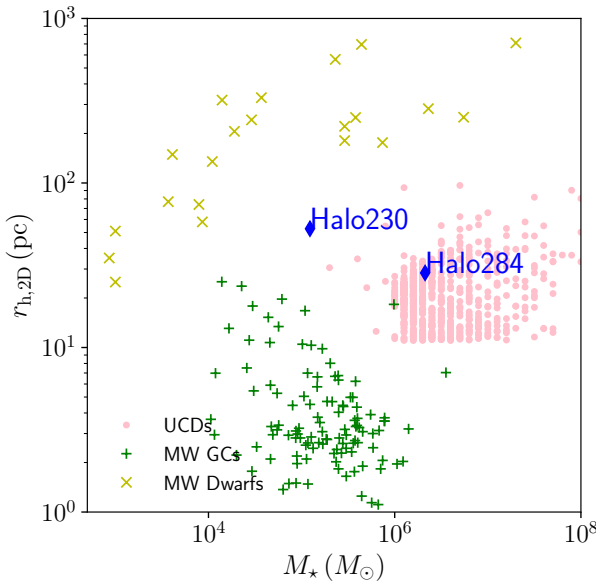


Fig. 12. Relation between the mass of galaxies and their projected half-mass radius. The yellow crosses and green pluses indicate dwarf galaxies (McConnachie 2012) in the local group and globular clusters in the Milky Way (Baumgardt & Hilker 2018), respectively. The pink dots indicate ultra-compact dwarfs (Liu et al. 2020), and the blue diamonds show our simulated galaxies. Alt text: Scatter plot for three types of stellar systems and simulated galaxies.

was located in the region of UCDs, rather than the satellites of the Milky Way. In the halos of Sureda et al. (2025), Halo D has the most compact stellar distribution in their samples. The stellar mass of their Halo D was $1.2 \times 10^6 M_\odot$, which is similar to our Halo 284, but their half-mass radius of 120 pc was larger than that of ours (28 pc). Different from their Halo A, which shows a steeper cusp than the DMO simulation, their Halo D did not show such a trend. In addition, the stellar-to-halo mass ratio of their Halo D was $< 10^{-3}$, which is lower than that of Halo 284.

As shown in Figure 5, the circular velocity of Halo 284 increased much faster than in Halo 230, and more stars were formed before the reionization epoch. Such an early evolution may have resulted in the formation of a UCD-like galaxy. However, the results of this study were obtained for only two halos, and therefore, more robust results would require similar simulations of other halos to see if there is any variation among galaxies.

5 Summary

In this study, we performed cosmological zoom-in simulations of dwarf galaxies of DM halos with masses of $\sim 10^9 M_\odot$ at $z=0$. The mass resolution was 19 and $102 M_\odot$ for gas and DM particles, respectively. The evolution of halo density profiles was investigated. One of our two dwarf galaxies (Halo 230) was similar to ultra-faint or classical dwarfs with a stellar-to-halo-mass ratio of $\sim 10^{-4}$. The DM density profile was not altered from that in the DM-only simulation, and the powers of the innermost slope were -1.07 and -0.88 for the DM-only and the Hydro simulations, respectively. Once the halo was formed, its profile remained unchanged over time. The other (Halo 284) had a larger stellar-to-halo mass ratio of $> 10^{-3}$, which is typical for galaxies with halos that are an order of magnitude more massive than those in our samples. This

galaxy was more compact compared to the satellites of the Milky Way and as compact as UCDs. The power of the DM halo profile with baryons was steeper (-1.94) than that of the DM-only simulation (-1.45). We did not find any cusp-to-core transition in our samples.

We also investigated the dependence of the galaxy structures on the resolution. In our low-resolution runs (Hydro Low), the stellar distribution of Halo 284 was more extended than that of Halo 230. In our high-resolution runs (Hydro), the half-mass radius of Halo 284 (28.4 pc) became smaller than that of Halo 230 (52.7 pc). The stellar masses were 2.12×10^6 and $1.23 \times 10^5 M_\odot$ for Halo 284 and 230, respectively. The mass and density of Halo 284 are comparable to those of UCDs, and we found it only in simulations with sufficiently high resolution. We further performed a higher-resolution simulation for Halo 284, although it is still in the early phase of star formation due to the calculation cost. This model maintained its compact structure even after starting supernova feedback. We, therefore, considered that the simulation results had converged.

The difference between these two dwarfs may come from the halo mass at the reionization epoch. Although the final halo mass is similar for both halos, the halo with a higher stellar mass (Halo 284) grows earlier than the other halo (Halo 230). The early growth of the halo mass before reionization makes the DM potential deep enough for the halo to continue star formation after reionization. Thus, the early evolution of the DM halo may be a necessary condition for the formation of UCDs.

Acknowledgments

Simulations and analyses in this study were carried out on Cray XC50 and analysis servers at the Center for Computational Astrophysics, National Astronomical Observatory of Japan, and Fujitsu PRIMERGY CX400M1/CX2550M5 (Oakbridge-CX) at the Supercomputer Division of the Information Technology Center, The University of Tokyo. We thank Kohei Hayashi for providing the observational data of dwarf galaxies. We would like to thank Editage (www.editage.jp) for English language editing.

Funding

This research was supported by KAKENHI Grant Numbers 23K22530, 21K03614, 21K03633, 22KJ0157, 22K03688, 24K07095, 25K01046, and 25H00664.

Data availability

The simulation data will be provided upon request.

Appendix 1 Comparison with a higher resolution simulation

In order to see the effect of the resolution, we performed an additional higher resolution simulation only for Halo 284 (model Halo 284 Hydro High). The resolutions for gas and DM particles are 2.37 and $12.8 M_\odot$, respectively. The gravitational softening lengths are 2.84 and 4.50 pc for the gas and DM. The time for the beginning of the star formation and the subsequent star formation rate of the Hydro High model were similar to those of the Hydro model, but the peak value of the star formation rate was slightly higher than that of the Hydro model (see Figure 4).

Table 4. Same as Table 4 but for the highest resolution one

Model	m_{gas} [M_{\odot}]	ϵ_{gas} [pc]	$m_{\text{DM, min}}$ [M_{\odot}]	$\epsilon_{\text{DM, min}}$ [pc]
Hydro High	2.37	2.84	12.8	4.50

From left to right: (1) gas-mass resolution (m_{gas}) (2) gas softening length (ϵ_{gas}) (3) minimum dark-matter mass ($m_{\text{DM, min}}$) (4) minimum dark-matter softening length ($\epsilon_{\text{DM, min}}$).

Due to the computational cost, we stopped the Hydro High simulation at $z = 8.72$ ($t = 0.568$ Gyr). A comparison of the halo and stellar distributions of these models was done at $z = 8.75$, and the results are summarized in Table 5. The stellar mass of the Hydro High model was approximately twice that of the Hydro model. The differences in the M_{\star}/M_{vir} ratio between these two models reflected those in their stellar masses. The half-mass decreased when we increased the resolution from Hydro High to Hydro, but it did not decrease further. The half-mass density of the Hydro model ($5.8 \times M_{\odot} \text{ pc}^{-3}$) was much higher than that of the Hydro Low model ($0.14 M_{\odot} \text{ pc}^{-3}$) but similar to that of the Hydro High model ($7.1 \times M_{\odot} \text{ pc}^{-3}$). Therefore, we consider that the results of our Hydro model converged, although the mass and density changed by a factor of two.

Because of the finite number of particles, the resolution of the simulations may affect the cusp of the innermost region of the DM halo. We estimated the convergence radius over which the radial density profile was considered to converge to higher-resolution simulations. Inside it, the DM density profile could become shallower due to two-body relaxation. The convergence radius was calculated using the criterion suggested in Power et al. (2003):

$$\frac{t_{\text{relax}}(r)}{t} = \frac{\sqrt{200}}{8} \frac{N(< r)}{\ln N(< r)} \left(\frac{\bar{\rho}(< r)}{\rho_{\text{crit}}} \right)^{-1/2} > 0.6, \quad (\text{A1})$$

where $N(< r)$ and $\bar{\rho}(< r)$ are the number of particles within a sphere of radius r and the average density in the sphere, respectively. For the critical density, $\rho_{\text{crit}} = 3H^2/8\pi G$, where H and G are the Hubble parameter and gravitational constant, respectively. If this criterion is satisfied, the relaxation time is longer than the age of the Universe, and therefore, the condition for the collisionless system is satisfied. We defined the minimum radius satisfying this criterion as the convergence radius, R_{conv} . Other definitions, such as 2 % of the viral radius, are also used (e.g., Schaller et al. 2015; Tollet et al. 2016), and they are smaller than that of Power et al. (2003).

Figure 14 shows the density profiles of the DM halo together with the convergence radii, R_{conv} , obtained using equation (A1) for the Hydro and Hydro High models. As shown in the figure, the density profiles differ even outside the convergence radius. The density of the DM halo for the Hydro High model is higher than that of the Hydro model because of the higher stellar mass in the central region. Although the density of the Hydro High model is higher than that of the Hydro model, the power of the density profile just outside the convergence radius is similar for both models.

Figure 15 shows the density profiles of the gas, star, and DM components of Halo 284 at $t = 0.568$ Gyr ($z = 8.72$). Although the innermost region densities are higher in the Hydro High model, the characteristics of the three components are consistent: the DM and star densities are comparable, and the gas has a flat distribution in the central region. Thus, we consider that the Hydro simulation resolves the inner cusp in our simulations.

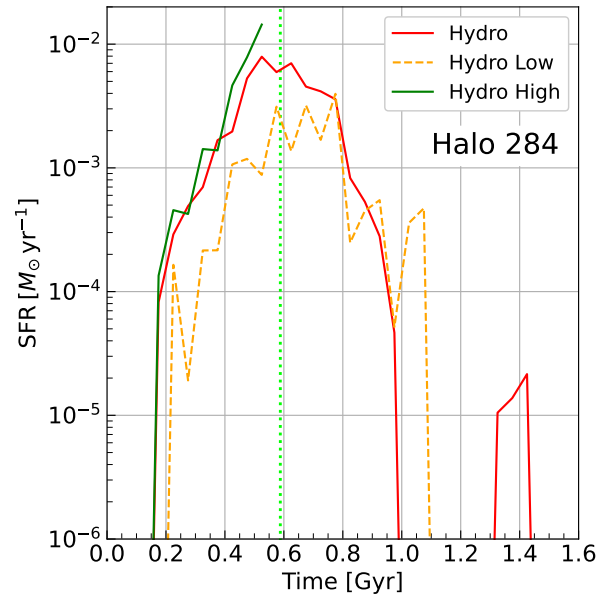


Fig. 13. Same as the bottom panel of Fig. 4, but with Hydro High. Alt text: Three-line figure. Red, orange, and green indicate Hydro, Hydro Low, and Hydro High models.

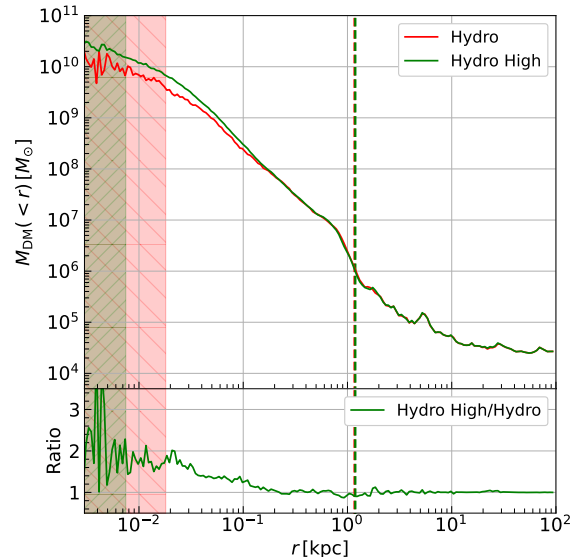
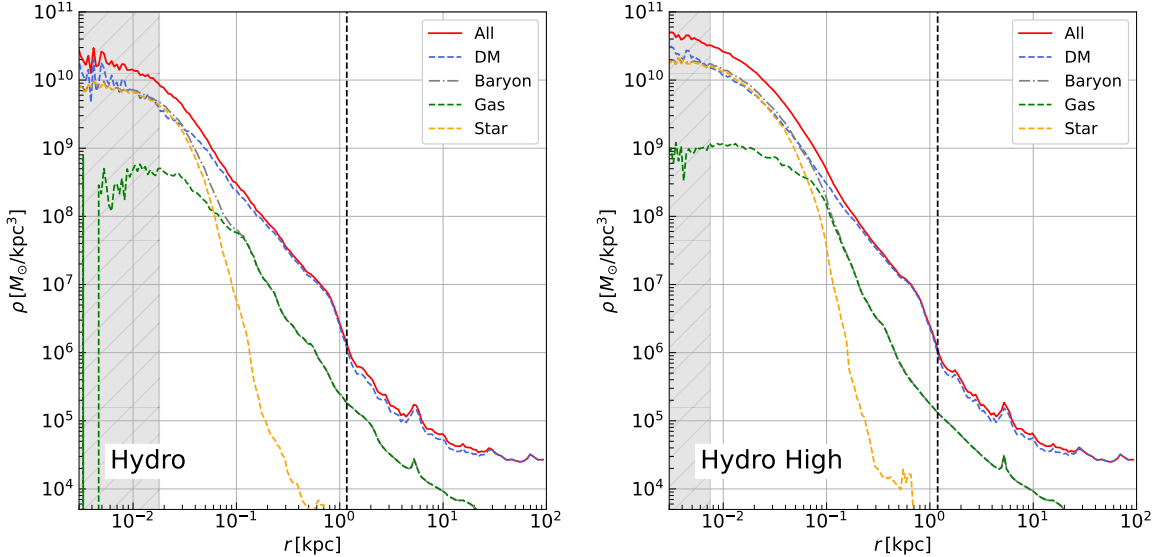


Fig. 14. DM density profiles (top) and their ratios (bottom) at $z = 8.72$ in the Hydro and Hydro High models of Halo 284. The red and green shaded regions indicate the conversion radii. The vertical dashed lines indicate the virial radii. Alt text: Two-line figure with red (Hydro) and green (Hydro High) lines.

Table 5. Properties of the dwarf galaxies at $z = 8.72$ ($t = 0.568$ Gyr). The columns are the same as in Table 3.

Halo Number	Model	$M_{\text{vir}} [M_{\odot}]$	$R_{\text{vir}} [\text{kpc}]$	$M_{\star} [M_{\odot}]$	$R_{1/2}^{3D} [\text{pc}]$	$R_{1/2}^{2D} [\text{pc}]$	$V_{\text{max}} [\text{km/s}]$	M_{\star}/M_{vir}
284	Hydro Low	4.78×10^7	1.16	1.98×10^5	69.7	55.4	13.8	4.14×10^{-3}
	Hydro	4.90×10^7	1.17	8.22×10^5	32.4	25.2	14.0	1.68×10^{-2}
	Hydro High	5.14×10^7	1.19	2.12×10^6	41.5	31.8	17.0	4.12×10^{-2}

**Fig. 15.** Density profiles of gas, star, and DM at $z = 8.72$ ($t = 0.568$ Gyr) for the Hydro (left) and Hydro High (right) models of Halo 284. The vertical black dashed line indicates the virial radius. Alt text: Two-panel figures with five lines for each. The colors are the same as Fig. 6.

Appendix 2 Halo profile fitting

In this study, we measured the power-law slope, α , at $1-2 R_{\text{conv}}$, which was the innermost region in our simulations similar to Sureda et al. (2025). On the other hand, $1-2\%$ of the viral radius at $z = 0$, $R_{\text{vir}}(z = 0)$, was often used in previous studies (Di Cintio et al. 2014; Tollet et al. 2016; Lazar et al. 2020). Figure 16 presents the power-law index of our DM halos fitted at $1-2\%$ of $R_{\text{vir}}(z = 0)$, similar to the previous studies. The x range of the lines indicates $R_{\text{vir}}(z = 0)$. As seen in this figure, $1-2\%$ of $R_{\text{vir}}(z = 0)$ is outside the central cusp region, and therefore the fitted slope is much steeper than the values we obtained for $1-2 R_{\text{conv}}$, except for the slope of the Halo 284 Hydro model, which is slightly steeper at $1-2 R_{\text{conv}}$ than that at $1-2\%$ of $R_{\text{vir}}(z = 0)$. For Halo 230, $1-2\%$ of $R_{\text{vir}}(z = 0)$ is obviously outside the central cusp. From these results, we adopted $1-2 R_{\text{conv}}$ to measure the power-law slope of the cusp. The resolution of Sureda et al. (2025) was higher than ours. In such cases, $1-2\%$ of R_{vir} is far from the convergence radius. Therefore, $1-2\%$ of R_{vir} is not sufficiently small to capture the power of the central cusp. However, the power measured at $1-2 R_{\text{conv}}$ changes as the convergence radius changes with time, as shown in Fig. 9.

Appendix 3 Previous simulations

Figure 10 plots the relation between the stellar-to-halo mass ratio and the power-law slope of the DM halo obtained from previous numerical studies (Di Cintio et al. 2014; Tollet et al. 2016; Lazar et al. 2020) as the green, blue, and red shaded regions, respectively. These regions were obtained by fitting their results using

the following functions:

$$\alpha(x) = n - \log_{10} \left[\left(\frac{x}{x_0} \right)^{-\beta} + \left(\frac{x}{x_0} \right)^\gamma \right] \quad (\text{A2})$$

and

$$\alpha(x) = n - \log_{10} \left[n_1 \left(1 + \frac{x}{x_1} \right)^{-\beta} + \left(\frac{x}{x_0} \right)^\gamma \right] \quad (\text{A3})$$

where $x = M_{\star}/M_{\text{halo}}$, and $n, n_1, x_0, x_1, \beta, \gamma$ are fitting parameters. We used eq. (A2) for the result of Di Cintio et al. (2014) and eq. (A3) for those of Tollet et al. (2016) and Lazar et al. (2020). The fitting parameters are summarized in Table 6, and we have taken $\Delta\alpha = 0.2$ for all vertical widths.

References

Agertz, O., Pontzen, A., Read, J. I., et al. 2020, MNRAS, 491, 1656,
 Barnes, J., & Hut, P. 1986, Nature, 324, 446,
 Baumgardt, H., & Hilker, M. 2018, MNRAS, 478, 1520,
 Behroozi, P. S., Wechsler, R. H., & Conroy, C. 2013, ApJ, 770, 57,
 Bullock, J. S., & Boylan-Kolchin, M. 2017, ARA&A, 55, 343,
 Burkert, A. 1995, ApJL, 447, L25,
 de Blok, W. J. G. 2010, Advances in Astronomy, 2010, 1,
 Di Cintio, A., Brook, C. B., Dutton, A. A., et al. 2014, Monthly Notices of the Royal Astronomical Society, 441, 2986,
 Di Cintio, A., Brook, C. B., Macciò, A. V., et al. 2014, MNRAS, 437, 415,
 Dutton, A. A., Buck, T., Macciò, A. V., et al. 2020, Monthly Notices of the Royal Astronomical Society, 499, 2648,
 Ferland, G. J., Korista, K. T., Verner, D. A., et al. 1998, Publications of the Astronomical Society of the Pacific, 110, 761,
 Ferland, G. J., Porter, R. L., van Hoof, P. A. M., et al. 2013, Revista mexicana

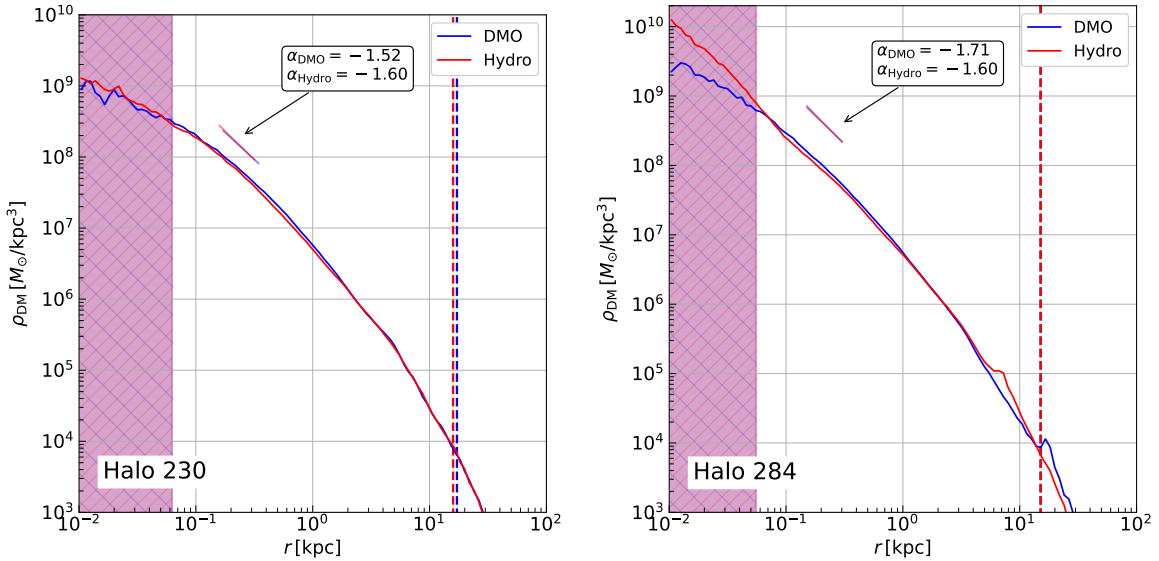


Fig. 16. Same as Figure 8 but fitted for 1–2% virial radius at $z = 0$, $R_{\text{vir}}(z = 0)$, for Halo 230 (left) and Halo 284 (right). The red and blue lines indicate the power-law slope and the range of 1–2% $R_{\text{vir}}(z = 0)$. Alt text: Two-panel plot with two lines for each. Blue and Red indicate DMO and Hydro models, respectively. The fitted powers are -1.52 and -1.60 for DMO and Hydro, respectively, in Halo 230. They are -1.71 and -1.68 for DMO and Hydro, respectively, in Halo 284.

Table 6. Parameter values of the fitting functions for previous simulations.

Paper	Function	n	n_1	x_0	x_1	β	γ
Di Cintio et al. (2014)	eq. A2	0.132	-	8.89×10^{-3}	-	0.593	1.99
Tollet et al. (2016)	eq. A3	-0.158	26.49	8.77×10^{-3}	9.44×10^{-5}	0.85	1.66
Lazar et al. (2020)	eq. A3	-1.60	0.80	9.18×10^{-2}	6.54×10^{-3}	5	1.05

de astronomía y astrofísica, 49, 137,
 Ferland, G. J., Chatzikos, M., Guzmán, F., et al. 2017, Revista mexicana de astronomía y astrofísica, 53, 385,
 Fitts, A., Boylan-Kolchin, M., Elbert, O. D., et al. 2017, Monthly Notices of the Royal Astronomical Society, 471, 3547,
 Flores, R. A., & Primack, J. R. 1994, The Astrophysical Journal, 427, L1,
 Fujii, M. S., Saitoh, T. R., Hirai, Y., & Wang, L. 2021, PASJ, 73, 1074,
 Governato, F., Brook, C., Mayer, L., et al. 2010, Nature, 463, 203,
 Griffen, B. F., Ji, A. P., Dooley, G. A., et al. 2016, The Astrophysical Journal, 818, 10,
 Gutcke, T. A., Pakmor, R., Naab, T., & Springel, V. 2021, MNRAS, 501, 5597,
 Haardt, F., & Madau, P. 2012, The Astrophysical Journal, 746, 125,
 Hahn, O., & Abel, T. 2011, Monthly Notices of the Royal Astronomical Society, 415, 2101,
 Hayashi, K., Chiba, M., & Ishiyama, T. 2020, The Astrophysical Journal, 904, 45,
 Hayashi, K., Hirai, Y., Chiba, M., & Ishiyama, T. 2023, ApJ, 953, 185,
 Hayashi, K., Kaneda, Y., Mori, M., & Shinozaki, M. 2025, arXiv e-prints, arXiv:2507.22155,
 Hirai, Y., Fujii, M. S., & Saitoh, T. R. 2021, Publications of the Astronomical Society of Japan, 73, 1036,
 Hirai, Y., Saitoh, T. R., Fujii, M. S., Kaneko, K., & Beers, T. C. 2025, ApJL, 980, L25,
 Hopkins, P. F., Wetzel, A., Kereš, D., et al. 2018, Monthly Notices of the Royal Astronomical Society, 480, 800,
 Hu, C.-Y. 2019, MNRAS, 483, 3363,
 Kaneda, Y., Mori, M., & Otaki, K. 2024, PASJ, 76, 1026,
 Katz, N. 1992, The Astrophysical Journal, 391, 502,
 Klypin, A., & Holtzman, J. 1997, arXiv,
 Knollmann, S. R., & Knebe, A. 2009, The Astrophysical Journal Supplement Series, 182, 608,
 Lazar, A., Bullock, J. S., Boylan-Kolchin, M., et al. 2020, Monthly Notices of the Royal Astronomical Society, 497, 2393,
 Liu, C., Côté, P., Peng, E. W., et al. 2020, ApJS, 250, 17,
 McConnachie, A. W. 2012, AJ, 144, 4,
 Moore, B. 1994, Nature, 370, 629,
 Moster, B. P., Naab, T., & White, S. D. M. 2013, MNRAS, 428, 3121,
 Muni, C., Pontzen, A., Read, J. I., et al. 2025, MNRAS, 536, 314,
 Navarro, J. F., Frenk, C. S., & White, S. D. M. 1996, The Astrophysical Journal, 462, 563,
 Navarro, J. F., Hayashi, E., Power, C., et al. 2004, Monthly Notices of the Royal Astronomical Society, 349, 1039,
 Nomoto, K., Kobayashi, C., & Tominaga, N. 2013, ARA&A, 51, 457,
 Ogiya, G., & Mori, M. 2014, ApJ, 793, 46,
 Oh, S.-H., de Blok, W. J. G., Brinks, E., Walter, F., & Kennicutt, Jr., R. C. 2011, AJ, 141, 193,
 Okamoto, T., & Frenk, C. S. 2009, MNRAS, 399, L174,
 Oman, K. A., Navarro, J. F., Fattahi, A., et al. 2015, MNRAS, 452, 3650,
 Orkney, M. D. A., Read, J. I., Rey, M. P., et al. 2021, MNRAS, 504, 3509,
 Orkney, M. D. A., Read, J. I., Rey, M. P., et al. 2021, Monthly Notices of the Royal Astronomical Society, 504, 3509,
 Planck Collaboration, Aghanim, N., Akrami, Y., et al. 2020, Astronomy & Astrophysics, 641, A6,
 Pontzen, A., & Governato, F. 2012, MNRAS, 421, 3464,
 Portinari, L., Chiosi, C., & Bressan, A. 1998, Astronomy & Astrophysics, 334, 505,
 Power, C., Navarro, J. F., Jenkins, A., et al. 2003, Monthly Notices of the Royal Astronomical Society, 338, 14,
 Rahmati, A., Pawlik, A. H., Raičević, M., & Schaye, J. 2013, Monthly Notices of the Royal Astronomical Society, 430, 2427,
 Revaz, Y., & Jablonka, P. 2018, A&A, 616, A96,

Saitoh, T. R. 2017, *The Astronomical Journal*, 153, 85,
Saitoh, T. R., Daisaka, H., Kokubo, E., et al. 2008, *Publications of the Astronomical Society of Japan*, 60, 667,
—. 2009, *Publications of the Astronomical Society of Japan*, 61, 481,
Saitoh, T. R., & Makino, J. 2013, *The Astrophysical Journal*, 768, 44,
Sales, L. V., Wetzel, A., & Fattahi, A. 2022, *Nature Astronomy*, 6, 897,
Salpeter, E. E. 1955, *The Astrophysical Journal*, 121, 161,
Schaller, M., Frenk, C. S., Bower, R. G., et al. 2015, *Monthly Notices of the Royal Astronomical Society*, 451, 1247,
Schmidt, M. 1959, *The Astrophysical Journal*, 129, 243,
Springel, V. 2005, *Monthly Notices of the Royal Astronomical Society*, 364, 1105,
Springel, V., White, S. D. M., Jenkins, A., et al. 2005, *Nature*, 435, 629,
Sureda, J., Brown, S. T., Fattahi, A., et al. 2025, *arXiv e-prints*, arXiv:2511.10582,
Tegmark, M., Blanton, M. R., Strauss, M. A., et al. 2004, *The Astrophysical Journal*, 606, 702,
Tollet, E., Macciò, A. V., Dutton, A. A., et al. 2016, *Monthly Notices of the Royal Astronomical Society*, 456, 3542,
Wheeler, C., Hopkins, P. F., Pace, A. B., et al. 2019, *Monthly Notices of the Royal Astronomical Society*, 490, 4447,